Journal of Materials Chemistry A

ROYAL SOCIETY OF CHEMISTRY

PAPER

View Article Online
View Journal | View Issue

Cite this: J. Mater. Chem. A, 2024, 12, 33898

Metal-ion-coordinated cross-linked quasi-solid-state polymer electrolyte for a high energy-density and long-life Prussian blue analogs cathode†

Xinyu Wang,[ab] Cheng Yang,*[a] Ning Jiang,[ab] Yichao Wang,[ab] Shouyu Sun[ab] and Yu Liu *[a]

As one of the most promising cathode materials for sodium-ion batteries, Prussian blue analogs (PBAs) cathodes face challenges in terms of poor cycling stability owing to their poor interfacial stability. Poor interfacial stability often leads to irreversible behaviors such as dissolution of cathode transition metals and catalytic decomposition of solvents. Herein, a novel metal ion-coordinated cross-linked quasi-solid-state polymer electrolyte was prepared *via* an *in situ* method using a four-armed cross-linker, where the denser and more efficient three-dimensional network renders the electrolyte with excellent chemical and electrochemical stabilities, minimizes catalytic decomposition side reactions and improves the interfacial stability of high-voltage PBAs cathodes. Moreover, the combination of *in situ* technology with Ti-MOFs fillers affords a highly compatible electrode/electrolyte interphase and an organic/inorganic composite Na^+ conduction pathway, which accelerates Na^+ transport and enhances interfacial stability. Thus, the as-designed polymer electrolyte exhibits an ionic conductivity of 3.85 mS cm^{-1} and extended oxidation stability of 5.1 V, coupled with improved mechanical strength and safety. The CFM-PBAs||Na battery demonstrates excellent rate performance and cycling stability (with an average coulombic efficiency of nearly 100% over 2000 cycles). Furthermore, the high-capacity FM-PBAs||Na battery achieves an ultra-high energy density of 445 Wh kg^{-1}, showcasing significant potential for high energy-density and long-life PBAs cathodes.

Received 18th July 2024
Accepted 17th September 2024

DOI: 10.1039/d4ta04988h

rsc.li/materials-a

1 Introduction

In recent years, sodium-ion batteries (SIBs) have shown tremendous potential for large-scale energy storage applications owing to their advantages such as abundant resource availability, wide operating temperature range, and high energy density.[1–6] However, the energy density of SIBs is still insufficient to meet the demands of current practical applications.[7–10] To develop high energy-density SIBs, researchers have focused on exploring various cathode materials with high capacity and voltage platform.[11–14] Among them, Prussian blue analogs (PBAs) have garnered significant attention from researchers for their low cost, high capacity, and excellent rate performance.[15–17] Nevertheless, in practical applications, PBAs cathodes experience severe cycling degradation due to the lack of a stable electrode/electrolyte interphase.[18,19] Extensive research has demonstrated that apart from the cathode material itself, different electrolytes play a pivotal role in the cycling stability of PBAs cathodes, which cannot be overlooked.[20,21]

In previous research works, PBAs-based cathodes were often paired with liquid electrolytes,[22–24] but they frequently suffered from structural degradation caused by the dissolution of metal ions, leading to issues such as rapid capacity decay and short cycling lifespan. This was primarily attributed to uncontrolled side reactions such as the decomposition of solvents at the interphase during the insertion and extraction of Na^+. Researchers often utilized additives[22,25] or created high-concentration electrolytes[24] to improve the cathode/electrolyte interphase. However, these methods still struggle to address the issues faced during large-scale applications. On the one hand, it is difficult to control the reaction extent of additives,[26] and the formed electrode/electrolyte interphase has a low homogeneity.[27] On the other hand, high-concentration electrolytes sacrifice intrinsically limited ionic conductivity[28] and cannot solve the problem of solvent decomposition fundamentally. At present, the regulation strategies for liquid electrolytes fail to solve the problem of cycling failure of PBAs cathodes thoroughly, which are still limited by uncontrollable interface behavior and severe dissolution of transition metals, making practical applications difficult.

[a]Shanghai Institute of Ceramics, Chinese Academy of Sciences, Shanghai 200050, China. E-mail: yangcheng@mail.sic.ac.cn; yuliu@mail.sic.ac.cn

[b]University of Chinese Academy of Sciences, Beijing 100049, China

† Electronic supplementary information (ESI) available. See DOI: https://doi.org/10.1039/d4ta04988h

Compared to traditional liquid electrolytes, quasi-solid-state polymer electrolytes (QSPEs), with their excellent mechanical strength, thermal stability, extremely low volatility, and high chemical/electrochemical stability, are considered a promising strategy to replace liquid electrolytes and achieve the long-term cycling of SIBs.[29] As an intermediate state between liquid and solid electrolytes, QSPEs are wrapped in the liquid components by a polymer network to become a gel state. Consequently, the mobility of liquid plasticizers is restricted, which helps inhibit side reactions at the interphases and enhance the interfacial stability.[30–34] Currently, researches on QSPEs mainly focus on inhibiting dendrite formation on sodium metal[31] and enhancing interfacial stability and have made significant progress. However, due to their unique structural characteristics, the transport of Na^+ in QSPEs is no longer dominated by the liquid phase but occurs within the swollen gel phase or liquid phase. The mobility of polymer segments also determines the level of Na^+ movement to a certain extent, resulting in significant shortcomings in ionic conductivity[33,34] and interfacial compatibility between QSPEs and liquid electrolytes. Unfortunately, QSPEs struggle to meet the requirements for cycling stability and high energy density of PBAs cathodes, which still need more in-depth research.

Herein, we designed a metal ions-coordinated cross-linked quasi-solid-state polymer electrolyte tailored for fast-charging PBAs cathodes through *in situ* polymerization technology. Distinct from conventional polymer electrolytes, we innovatively introduced four-armed cross-linker penaeryhrioleraacrylae (PETEA) and metal–organic framework fillers (Ti-MOFs), which altered the Na^+ migration behavior and improved the cathode electrode/electrolyte interphase stability. The designed cross-linked quasi-solid-state polymer electrolyte has multiple advantages: (a) PETEA with four C=C bonds, innovatively used as a cross-linker to efficiently construct a three-dimensional crosslinked network, which reduces the activity of solvents, provides the electrolyte with excellent chemical and electrochemical stability, minimizes the occurrence of catalytic decomposition side reactions and improves the interfacial stability of PBAs cathodes. (b) The combination of the *in situ* method with Ti-MOFs inorganic fillers working as anchor points constructs a high-quality polymer network, realizing a highly compatible electrode/electrolyte interphase and an organic/inorganic composite Na^+ conduction pathway, which accelerates Na^+ transport and optimizes the interfacial stability. (c) Ti-MOFs renders the electrolyte with good mechanical strength and high-voltage resistance.[35] Thus, the as-designed polymer electrolyte demonstrates an excellent ionic conductivity (3.85 mS cm^{-1}), superior oxidation stability (5.1 V), coupled with improved mechanical strength and safety. The symmetric battery exhibits stable cycling for over 800 hours at a current density of 0.2 mA cm^{-2}. The CFM-PBAs||Na battery achieves long-term cycling exceeding 2000 cycles (500 mA g^{-1}) with a coulombic efficiency close to 100%. The high-capacity FM-PBAs||Na battery realizes an impressive energy density of up to 445 Wh kg^{-1}, offering a new perspective for achieving high energy density and fast-charging targets with PBAs cathodes.

2 Results and discussion

Metal–organic frameworks possess various advantages, including high specific surface area, diverse and designable microstructures, making them suitable as fillers for polymer electrolytes.[35] Ti-MOFs prepared *via* the solvothermal method can play dual functions (Fig. S1†). On the one hand, their organic components can be highly compatible with polymer monomers,[36] which can work as anchor points and construct an organic/inorganic composite Na^+ conduction channel. On the other hand, these Ti-MOFs with abundant O sites can facilitate the migration of Na^+ within the polymer electrolyte, making it an excellent choice for enhancing the ionic conductivity for QSPE.[37] Fig. 1b shows that the XRD pattern of the synthesized Ti-MOFs is consistent with previous research results,[38–40] confirming their construction from Ti_8O_8 octahedra and organic ligands $O_2C–C_6H_4–CO_2$. Additionally, the N_2 adsorption–desorption isotherms and pore size distribution of Ti-MOFs are presented in Fig. 1c. The Brunauer–Emmett–Teller (BET) specific surface area of Ti-MOFs is 29 $m^2 g^{-1}$, and the calculated Barrett–Joyner–Halenda (BJH) average pore diameter is 5.05 nm, indicating that Ti-MOFs possess a nanoscale porous structure.

Fig. 1a illustrates the one-step synthesis method of the quasi-solid-state polymer electrolyte. Initially, sodium salt ($NaClO_4$), solvent (PC), monomer (PEGDA), four-armed cross-linker (PETEA), and initiator (AIBN) were mixed at the designed ratio to prepare the precursor solution, designated as GPE. To protect the sodium metal anode and enhance the interfacial stability, a certain proportion of film-forming additive (FEC) and inorganic filler (Ti-MOFs) were added to the precursor solution, which was then designated as Ti@GPE. Subsequently, the precursor solution was injected onto the glass fiber membrane to assemble the coin batteries. Under heating conditions, the initiator triggers a free-radical polymerization reaction of C=C bonds, resulting in the formation of a three-dimensional cross-linked polymer network (Fig. S2†). A liquid electrolyte (1 M $NaClO_4$ PC) was used as the blank control group, labeled as LE. Notably, this process utilizes low-cost, eco-friendly PEGDA and PETEA as the polymerization monomer and cross-linker, respectively, and the *in situ* approach ensures high compatibility between the electrode and electrolyte, which is beneficial for reducing the interphase impedance. Fourier transform infrared (FT-IR) spectroscopy analysis was performed before and after polymerization (Fig. 1d and S3†). After thermal polymerization, the intensity of the characteristic peak at 1635 cm^{-1} attributed to C=C bonds in the monomers decreases significantly in the Ti@GPE electrolyte, directly confirming the successful polymerization.[41]

After thermal initiation and polymerization, the flowable liquid precursor solution transforms into a gel-like QSPE (Fig. S4†). These Al||Al symmetric batteries were assembled to evaluate the room-temperature ionic conductivity of different electrolytes (Fig. 2a). The LE electrolyte, with its high liquid mobility, exhibits an ionic conductivity of 4.51 mS cm^{-1}. In contrast, due to the limited mobility and low activity of

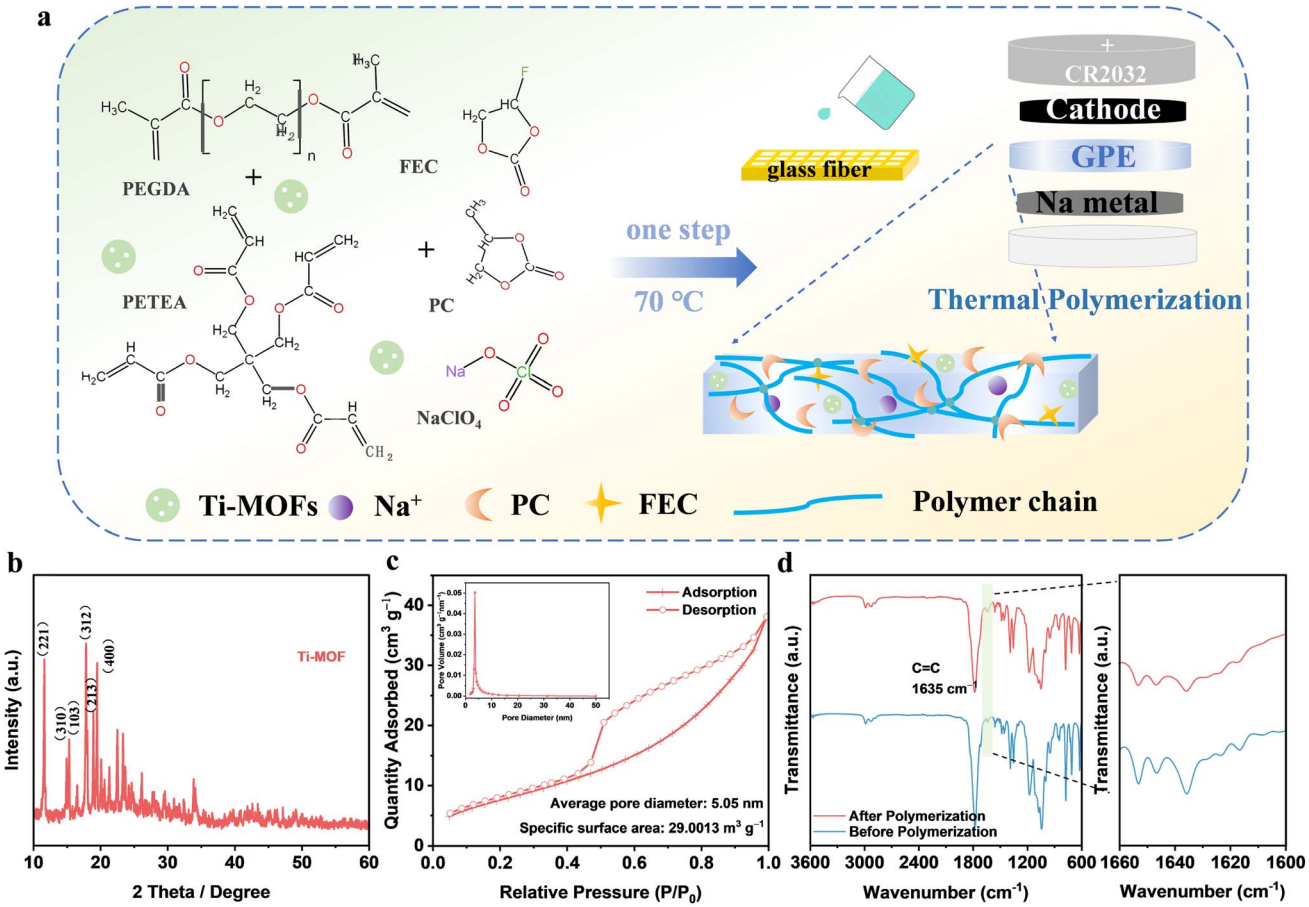

Fig. 1 Electrolyte and material preparation. (a) Schematic of the synthetic process of quasi-solid-state polymer electrolyte. (b) XRD and (c) BET of synthetic Ti-MOFs. (d) FT-IR spectra of the Ti@GPE polymer electrolyte before and after thermal polymerization.

solvents,[34] the ionic conductivity of GPE is 2.86 mS cm^{-1}. Nevertheless, these rich ether oxygen bonds in the PEGDA skeleton enable the rapid migration of Na^+, resulting in an ionic conductivity far superior to that of other QSPEs (Fig. 2f).[42] Notably, the addition of the Ti-MOFs filler leads to an organic/inorganic composite ion transport pathway, further enhancing the ionic conductivity to 3.85 mS cm^{-1}, nearly approaching the level of liquid electrolytes.[42] The temperature dependence of ionic conductivity follows the Arrhenius equation (Fig. 2b), and the impedance spectra is provided in Fig. S5.† As the temperature increases, the ionic conductivity of all the electrolytes is magnified. The activation energy required for Na^+ transport is 11.5 kJ mol^{-1} for Ti@GPE, lower than that of both the liquid electrolyte (13.32 kJ mol^{-1}) and GPE electrolyte (15.75 kJ mol^{-1}).[43] This may be attributed to the higher ionic conductivity and more efficient Na^+ transport channel induced by the Ti-MOFs filler.

Linear sweep voltammetry (LSV) is commonly used to estimate the electrochemical stability of the electrolytes. As shown in Fig. 2c and S6,† Ti@GPE exhibits the widest electrochemical window. The oxidation potential of Ti@GPE increases from 4.75 V for LE and 4.9 V for GPE to 5.1 V, indicating enhanced oxidation resistance and making it suitable for pairing with high-voltage cathodes. The enhanced oxidation stability is attributed to the limited activity of solvents by the long-chain polymer skeleton and the increased energy barrier for oxidative decomposition provided by FEC with a low HOMO energy level. The liquid precursor possesses high permeability to glass fibers. Ti@GPE not only exhibits excellent flexibility but also presents remarkable mechanical strength after polymerization. This impressive mechanical strength allows for rigorous 180° bending repeatedly without any visible cracks or damage, making it highly suitable for integration with flexible electrochemical devices (Fig. S7†). Fig. 2d presents the stress–strain curves of QSPEs. Ti@GPE demonstrates good strength and tensile performance, achieving a failure strain at 6% stress. This is attributed to the enhancement of the flexibility of the polymer skeleton by introducing Ti-MOFs to work as anchor points, thus improving the mobility of the polymer chains. Consequently, Ti@GPE can withstand a tensile stress of 13.85 MPa, which is beneficial for inhibiting the penetration of sodium dendrites.[44] Fig. 2e presents the thermogravimetric analysis curves for Ti@GPE, GPE and the pure glass fiber. QSPEs exhibit thermal decomposition temperatures higher than 320 °C, hinting at their superb thermal stability and improved safety.

The impact of Ti-MOFs-enhanced QSPE on Na plating/stripping behavior was evaluated through galvanostatic polarization tests in Na||Na symmetric batteries, as shown in Fig. 3a,

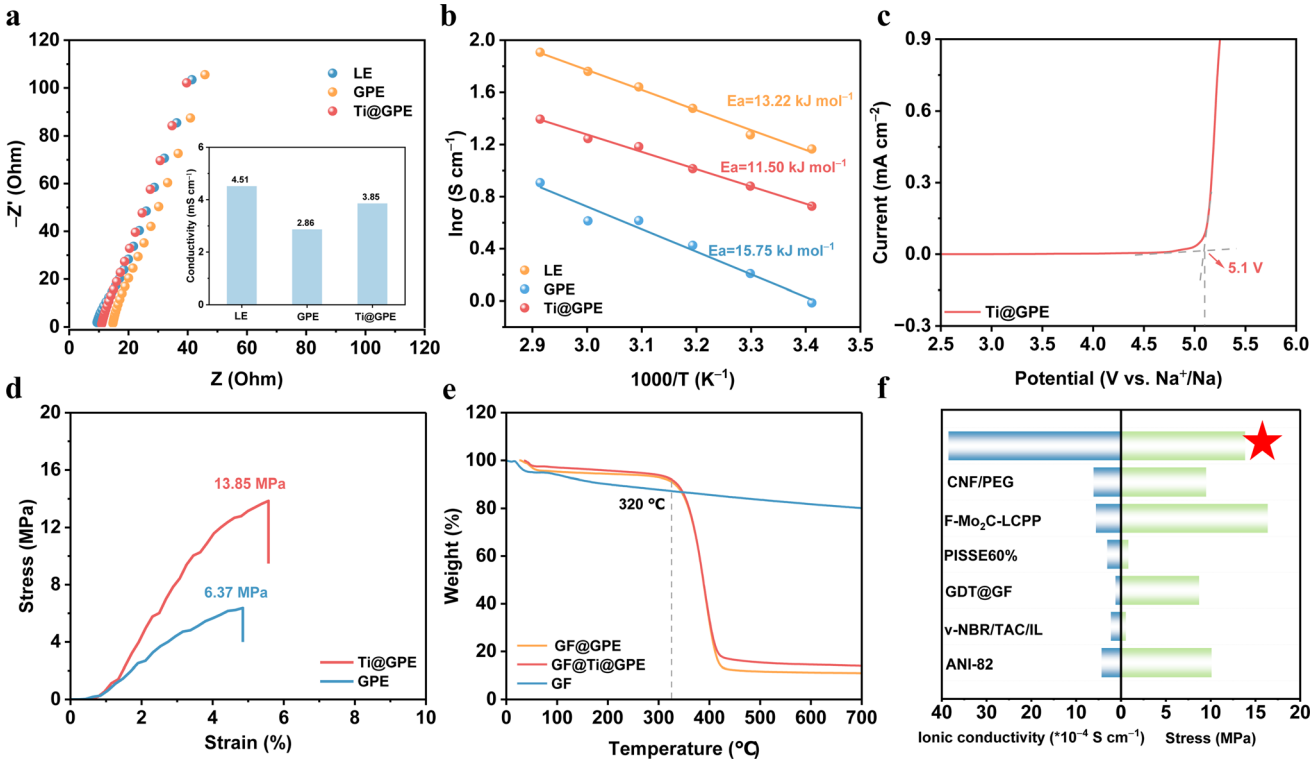

Fig. 2 The fundamental physicochemical properties of different electrolytes. (a) The ionic conductivity of different electrolytes. (b) Temperature dependency comparison of ionic conductivity for LE, GPE and Ti@GPE from 20 to 70 °C. (c) LSV curve of Ti@GPE. (d) The tensile performance and (e) TGA of glass fiber, GPE and Ti@GPE. (f) The comparison of the previously reported ionic conductivity and tensile strength of QSPEs with those reported in this work.

under a current density of 0.2 mA cm^{-2} and a deposition capacity of 0.2 mAh cm^{-2}. Although Na||LE||Na and Na||GPE||Na symmetric batteries exhibit relatively low initial polarization, their overpotentials rapidly increase to 1.2 V after 200 hours. This rapid increase is primarily attributed to the higher energy barriers for Na^+ transport, which is consistent with the fitting results of variable temperature conductivity at different temperatures (Fig. 2b). In contrast, the Na||Ti@GPE||Na symmetric battery demonstrates remarkable plating/stripping stability. The initial polarization voltage undergoes a slow decline, indicating an activation process that stabilizes after 20 hours. Throughout the 800 hour test, the Na||Ti@GPE||Na symmetric battery maintains a relatively stable overpotential of 150 mV. This outstanding performance signifies the excellent compatibility of Ti@GPE with Na metal. The superior compatibility can be attributed to several factors. Firstly, the intimate interfacial contact between the polymer electrolyte and Na metal facilitates efficient ion transfer and reduces interfacial resistance.[45] Secondly, the high specific surface area and microporous structure of Ti-MOFs are beneficial for accelerating the desolvation behavior of Na^+, which can balance sodium flux, inhibit dendrite growth, and promote uniform plating/stripping behavior.[46]

Fig. 3b depicts the cyclic voltammetry (CV) curves of these electrolytes by assembling Na||stainless steel asymmetric batteries. Ti@GPE polymer electrolyte exhibits enhanced reversibility throughout the plating/stripping process. Additionally, it possesses a considerable reduction current, indicating its superior Na^+ transport kinetics.[47] Fig. 3e presents the variable current cycling test conducted on the assembled Na||Ti@GPE||Na symmetric batteries. The battery underwent plating/stripping at 0.1, 0.2, 0.3, 0.4, and 0.5 mA cm^{-2} for 5 cycles at each current density and then returned to 0.2 mA cm^{-2}. Notably, for the Ti@GPE electrolyte, the polarization voltage only exhibits a slight increase in the first cycle with different current densities, followed by a subsequent decrease. Overall, the difference in the polarization voltage remains relatively small throughout the test. When the current density was restored to 0.2 mA cm^{-2}, the polarization voltage recovered to an even lower level than that before without short-circuit (Fig. S8†), enabling the symmetric battery to maintain plating/stripping stability. This phenomenon illustrates the remarkable rate capability of Ti@GPE with Na metal, even under fluctuating higher current densities. In contrast, the variable current test results for symmetric batteries paired with LE and GPE electrolytes show a gradual increase in overpotential with increasing durations (Fig. S9 and S10†). This is primarily attributed to the lack of a stable solid electrolyte interphase (SEI) between Na metal and the electrolyte, leading to continuous side reactions. These uncontrolled side reactions gradually increase the charge transfer resistance at the electrode/electrolyte interphase, which is reflected in the increase in the overpotential.

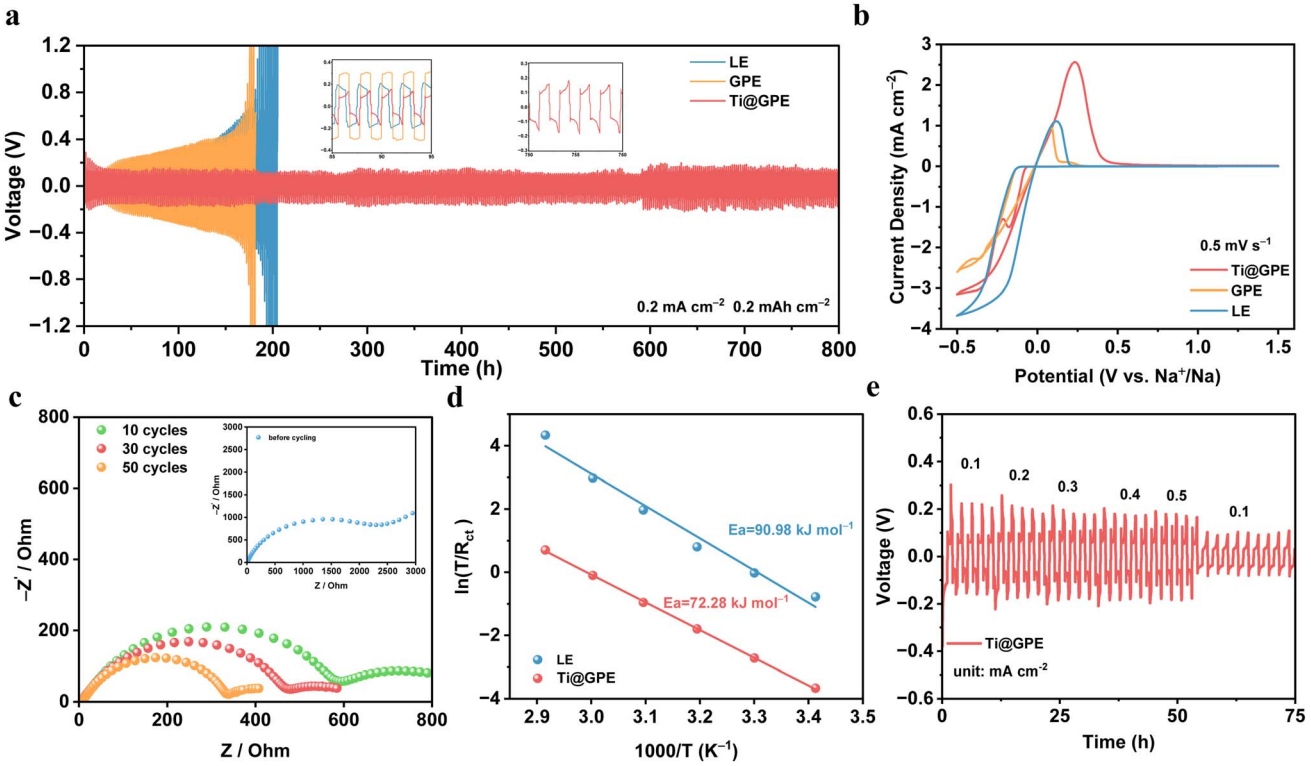

Fig. 3 The plating/stripping behavior of Na metal. (a) Galvanostatic cycling of Na||Na symmetric batteries at (a) 0.2 mA cm^{-2}/0.2 mAh cm^{-2}. (b) The CV curves of LE, GPE and Ti@GPE at a scanning rate of 0.5 mV s^{-1}. (c) EIS spectra of Na||Ti@GPE||Na with different durations and (d) kinetic energy barrier of Na^+ desolvation as calculated using Arrhenius analysis. (e) The rate performance of the Na||Ti@GPE||Na symmetric battery.

The electrochemical characteristics of the solid electrolyte interphase in symmetrical batteries with varying durations were characterized to validate the aforementioned conclusion. Fig. 3c and S11† present the electrochemical impedance spectra (EIS) of Na||Ti@GPE||Na, Na||LE||Na and Na||GPE||Na symmetric batteries at different durations. The impedance curves can be divided into two components: R_S, representing bulk electrolyte resistance and R_{SEI}, signifying reaction resistance at the electrode/electrolyte interphase. For Na||Ti@GPE||Na, the R_S and R_{SEI} of the symmetric battery decrease gradually as the cycling time increases (from approximately 2500 Ω to 330 Ω). This phenomenon is attributed to the enhanced interfacial contact and compatibility with Na metal after the initial activation of the SEI interphase, which demonstrates that the Ti@GPE electrolyte possesses a self-adapting effect. The Na^+ desolvation energy barrier (E_a) was calculated by the EIS results of the Na||LE||Na and Na||Ti@GPE||Na symmetric batteries at different temperatures (from 293 to 343 K). As depicted in Fig. 3d and S12,† the linear fitting of $\ln(T/R_{ct})$ *vs.* $1/T$ reveals that the calculated E_a of the Ti@GPE electrolyte (72.28 kJ mol^{-1}) is significantly lower than that of the LE electrolyte (90.98 kJ mol^{-1}), indicating the enhanced Na^+ desolvation rate,[48] which can accelerate the plating/stripping process of Na^+ and reduce polarization.

To investigate the feasibility of the designed Ti@GPE, copper–iron–manganese-based Prussian blue analogs (CFM-PBAs) cathode was chosen as the cathode to assemble batteries. Fig. 4a shows the initial three-cycle charge–discharge curves of CFM-PBAs||Ti@GPE||Na at a low current density of 0.2C (1C = 100 mAh g^{-1}). The CFM-PBAs||Ti@GPE||Na battery exhibits an initial discharge capacity of 92 mAh g^{-1}, with a slight increase in the second cycle, potentially due to the initial insufficient wettability of the pellet, which is gradually activated during the low-current cycling process. Compared to CFM-PBAs||Na batteries paired with LE and GPE electrolytes (Fig. S13†), Ti@GPE demonstrates a higher coulombic efficiency, which is attributed to the higher oxidation stability by introducing FEC with low HOMO energy level and faster Na^+ desolvation to inhibit the side decomposition of solvents. However, the LE and GPE electrolytes always maintain a low level of coulombic efficiency. Fig. 4b further presents the rate performance of batteries with different electrolytes with the current density from 0.2C to 10C. As the current density increases from 0.2C to 2C, there is only a slight decrease in the battery capacity. Also, reversible capacities of 73.6 mAh g^{-1}, 66.2 mAh g^{-1}, and 63.2 mAh g^{-1} were achieved at 5C, 8C, and 10C, respectively. In contrast, the capacity of LE and pure GPE electrolytes drops to about 30 mAh g^{-1} at 10C, primarily due to the excessive electrode/electrolyte impedance, which prevents the complete reaction of active materials. Moreover, when the current density returns to 1C, the reversible capacity of the Ti@GPE electrolyte recovers to 85.1 mAh g^{-1} and remains stable. The exceptional rate performance of the Ti@GPE-based battery is attributed to its outstanding ionic conductivity,

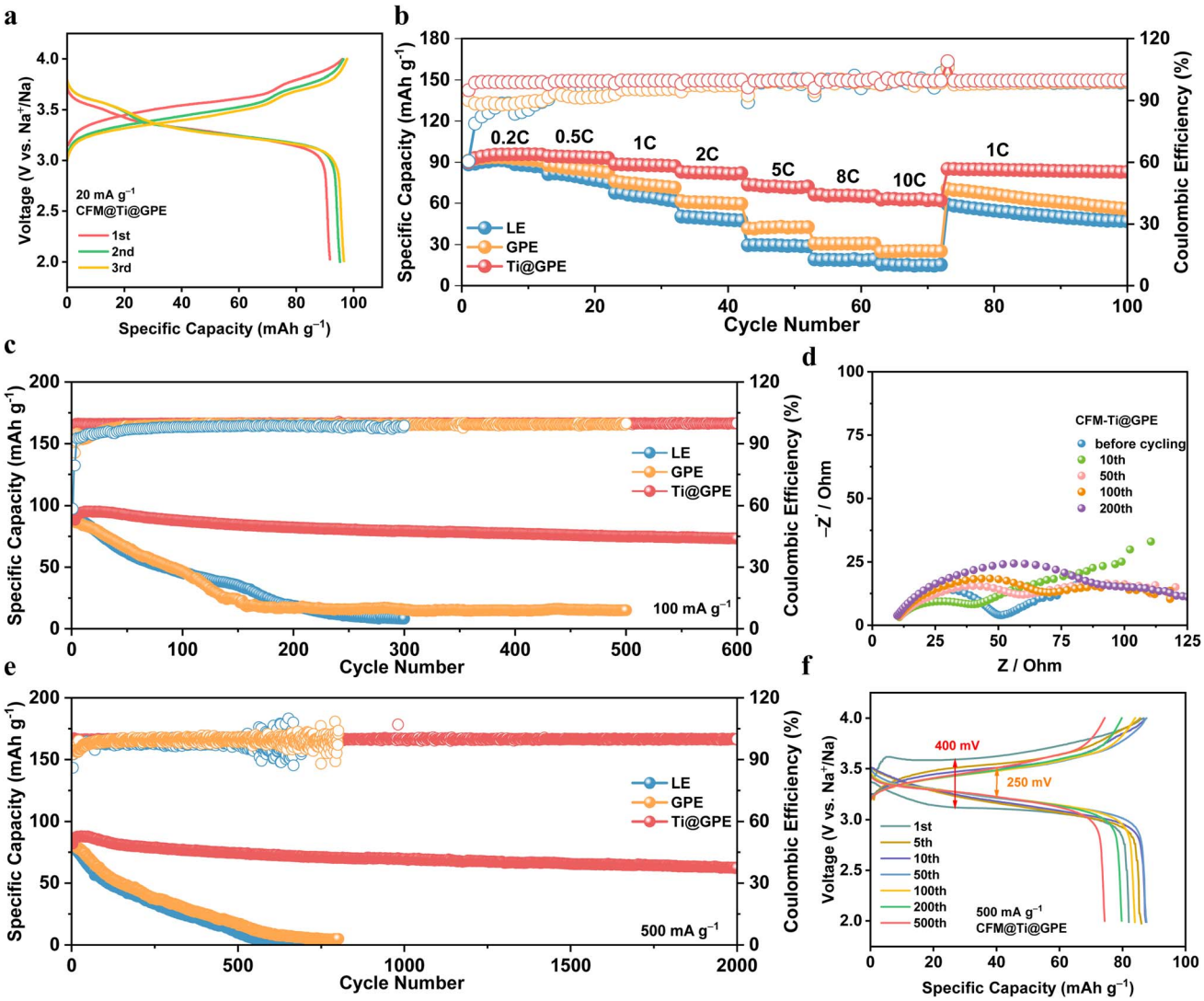

Fig. 4 The electrochemical performance of the CFM-PBAs||Na battery. (a) Initial three charge/discharge curves of Ti@GPE, (b) rate performance, (c and e) cycling performance at 1C and 5C of CFM-PBAs||Na with different electrolytes. (d) EIS curves of CFM-PBAs||Ti@GPE||Na after different cycling durations. (f) The charge/discharge curves of different cycles of CFM-PBAs||Na with Ti@GPE at 5C.

efficient ion transport channels and good interfacial compatibility between Ti@GPE and the PBAs cathode, ensuring the sufficient utilization of active materials. The corresponding charge–discharge curves shown in Fig. S14† demonstrate the well-maintained discharge platforms despite the current density fluctuating significantly in the CFM-PBAs||Ti@GPE||Na battery.

Long-term cycling tests can directly reflect the cycling performance improvement. Fig. 4c demonstrates that the CFM-PBAs||Na battery utilizing the Ti@GPE electrolyte exhibits superior cycling stability. Under 1C current density, these batteries with LE and pure GPE electrolytes show a gradual decay in the first 200 cycles, ultimately reaching less than 10% of their initial capacity. In stark contrast, the battery with the Ti@GPE electrolyte retains 83% of its capacity after 600 cycles, with an initial coulombic efficiency (ICE) of 95.1% and an average coulombic efficiency (ACE) of 99.8% (Fig. S15†). This is attributed to the highly compatible electrode/electrolyte interphase in the designed quasi-solid-state polymer electrolyte, which enables the excellent reversibility of electrode reactions. Furthermore, we tested the feasibility of applying the Ti@GPE polymer electrolyte at a higher current density. Consistent with the above results, the Ti@GPE electrolyte exhibits a higher ICE of 95.1% and ACE of 99.9% at a current density of 5C and retains 78% of its initial capacity after 2000 cycles, significantly outperforming the lifespan of CFM-PBAs cathodes in the LE electrolyte. Fig. 4f and S16† show the charge–discharge curves of CFM-PBAs||Na batteries with different electrolytes at 5C. During the first cycle, the initial polarization voltage of the Ti@GPE polymer electrolyte is as high as 400 mV, which may be related to the insufficient wetting of the polymer electrolyte on the PBAs cathode. However, with the increase in the cycling time, the discharge capacity increases gradually and tends to be stable, stabilizing the overall polarization voltage of the battery at 250 mV. This is attributed to the formation of a highly compatible electrode/electrolyte interphase, thus reducing the

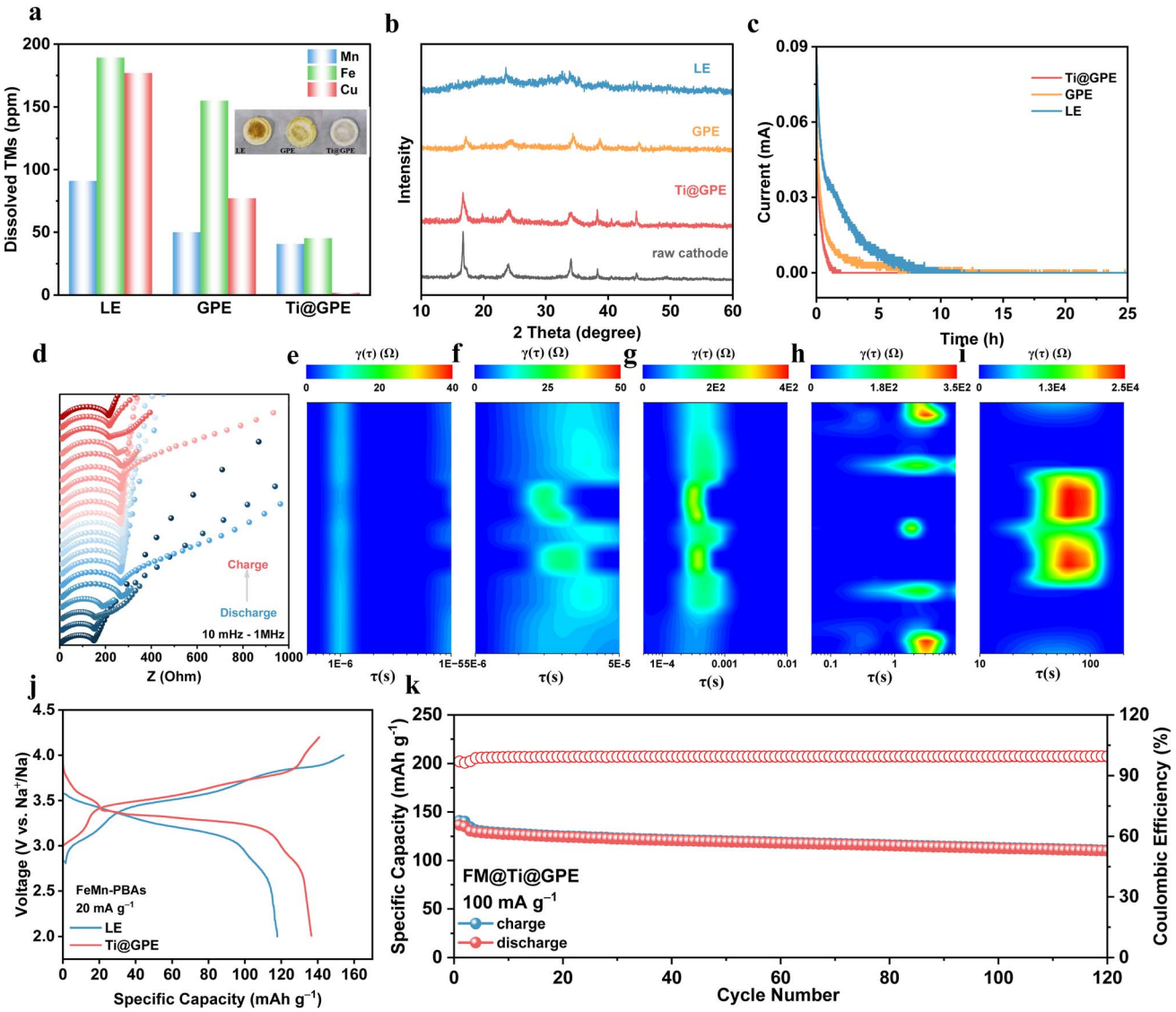

Fig. 5 The analysis of the electrode/electrolyte interphase and electrochemical performance of the FM-PBAs||Na battery. (a) Elemental analysis of dissolved transitional metal ions in different electrolytes after 1000 cycles (inset are photos of separators). (b) XRD of the cycled CFM-PBA cathode in different electrolytes and a raw cathode pellet. (c) The constant voltage float charge curves of CFM-PBAs||Na charged to 4.0 V for 24 h. (d–i) *In situ* GEIS and DRT of CFM-PBAs||Ti@GPE||Na during the charge/discharge process. (j) GCD and (k) long-term performance of the FM-PBAs||Ti@GPE||Na battery.

interfacial impedance. In contrast, due to its bad oxidation stability, the LE electrolyte fails to form a stable electrode/electrolyte interphase, leading to continuous decomposition of the solvents. Meanwhile, the GPE electrolyte experiences an increase in the gradual polarization due to poor interphase compatibility, even causing structural collapse of the cathodes and ultimately battery failure. The EIS tests of these batteries at different cycles also support this conclusion (Fig. 4d and S17†). The impedances of batteries with LE and GPE electrolytes increase exponentially, while the impedance in the Ti@GPE electrolyte remains low (less than 75 Ω). This directly proves that Ti@GPE facilitates the formation of an excellent electrode/electrolyte interphase, accelerating Na^+ migration and stabilizing the PBAs cathode.

More intuitively, it was found that the membranes cycled in LE and GPE electrolyte become yellow, and the content of copper, iron, and manganese transition metals in the residual electrolyte of separators is much higher than that in the Ti@GPE electrolyte (Fig. 5a). The dissolved transition metals indicate that the cathode has undergone severe structural degradation, which leads to cycling failure. In Fig. 5b, the cathodes cycled in the Ti@GPE electrolyte show significant differences in the peak intensity compared with the original cathode pellet. The decrease in the number and intensity of cathode peaks in both the LE and GPE systems indicates the collapse of the crystal structure, which verifies the above speculation directly.[49] The CFM-PBAs||Na battery was tested with a constant voltage float charge at 4 V to evaluate the parasitic

reactions between the cathode and different electrolytes. The Ti@GPE electrolyte significantly reduces the leakage current, indicating that there are fewer side reactions at the interphase. Fig. S18† shows that the CFM-PBAs||Ti@GPE||Na battery experiences less voltage drop during the static discharging test. The floating charge test and self-discharge test results show that Ti@GPE has good oxidation stability and can effectively inhibit interface parasitic reactions.[50,51]

Moreover, the *in situ* galvanostatic electrochemical impedance spectroscopy (*in situ*-GEIS) was employed to reveal the internal states related to different potentials (Fig. 5d), with a measurement interval of 0.2 V.[52] Throughout the charge–discharge process, the Ti@GPE electrolyte exhibits exceptional symmetry. To enhance the interpretation of the *in situ* GEIS spectra, the distribution of relaxation times (DRT) methodology was adopted. This method is advantageous for directly pinpointing the time constants associated with key electrochemical processes, significantly refining impedance analysis and greatly improving the precision of kinetic interpretations on the timescale. Fig. 5e–i and S19† depict the total timescale distributions of various kinetic processes of batteries utilizing Ti@GPE, LE and GPE electrolytes, corresponding to electronic conductivity, particle and current collector contact, cathode/electrolyte interphase, charge transfer at the interface, and solid-state diffusion in the electrodes, respectively.[53–55] Throughout the charge–discharge process, the Ti@GPE electrolyte displays a lower electronic conductivity resistance than LE but higher than that of the GPE electrolyte, consistent with the varying trends of ionic conductivity observed in different electrolytes. The wettability of the polymer electrolytes is inferior to that of liquid electrolytes, resulting in higher contact impedance between particles and the current collector. However, Ti-MOFs with high specific surface area provide more contact sites, enabling the Ti@GPE to exhibit lower contact impedance than the GPE electrolyte. Due to the exceptional oxidation stability of the Ti@GPE electrolyte, irreversible interfacial side reactions at the electrode/electrolyte interphase are suppressed, leading to a lower cathode/electrolyte interphase impedance and charge transfer impedance for Ti@GPE compared to LE, indicating the achievement of efficient stabilization at the electrode/electrolyte interphase with low side reactions activity. Additionally, the Ti@GPE electrolyte exhibits a lower Warburg diffusion impedance, which corresponds to a faster desolvation process of Na^+ at the electrode/electrolyte interphase, thereby facilitating lower diffusion energy barriers for Na^+.

The Ti@GPE design aims to enhance the energy density employing high energy-density PBAs cathodes. To validate the practical application potential of Ti@GPE, an iron–manganese-based PBAs (FM-PBAs) cathode with a higher specific capacity was tested. At a current density of 20 mA g^{-1}, the FM-PBAs||Na battery achieved an impressive specific capacity of 136.6 mAh g^{-1} (Fig. 5j), realizing an outstanding energy density of 445 Wh kg^{-1} (based on cathode mass). Furthermore, the FM-PBAs||Na battery demonstrates excellent cycling stability, retaining 84.25% of its capacity after 120 cycles at a current density of 100 mA g^{-1} (Fig. 5k), with an average coulombic efficiency as high as 98.6%. In contrast, the capacity retention of the LE electrolyte dropped to 24.74% after 120 cycles (Fig. S20†). These preliminary results indicate that Ti@GPE has the potential to address the cycling failure of PBAs cathodes, offering promising application prospects in large-scale energy storage.

3 Conclusion

In summary, we have successfully designed a metal ions-coordinated cross-linked quasi-solid-state polymer electrolyte through *in situ* methods, aiming to address the issue of transition metal dissolution and cycling failure caused by unstable electrode/electrolyte interphase of low-cost, high energy-density PBAs cathodes. We systematically investigated the impact of Ti-MOFs incorporation on the electrochemical performance of quasi-solid-state polymer electrolyte. The introduction of the low-cost, green, and safe polyethylene glycol polymer skeleton and four-armed cross-linker helped to limit the activity of solvents and suppress side reactions between the electrode and plasticizer. The as-designed QSPE endows the polymer electrolyte excellent chemical and electrochemical stability. Furthermore, combining *in situ* technology with Ti-MOFs inorganic fillers, we constructed an organic/inorganic composite channel, which enables the synergistic transport of Na^+ through different O sites, resulting in an ultra-high ionic conductivity of 3.85 mS cm^{-1}. With the incorporation of Ti-MOFs, the polymer electrolyte also achieved good mechanical strength (13.85 MPa) and high voltage resistance (5.1 V). The CFM-PBAs||Na batteries coupled with the as-designed Ti@GPE electrolyte exhibit excellent rate and cycling performance (2000 cycles), and the FM-PBAs||Na battery demonstrated a high-level energy density of 445 Wh kg^{-1}. This study provides new insights into the large-scale application of PBAs cathodes to achieve higher energy density and meet the demands of large-scale energy storage.

4 Experimental sections

4.1 Materials

Sodium perchlorate ($NaClO_4$, 99%, without water), propylene carbonate (PC, 99.7%, without water), fluoroethylene carbonate (FEC, >98%), poly(ethylene glycol) dimethacrylate (average M_n 550), penaeryhrioleraacrylae (PETEA, stab. with MEHQ, 80%), and 2,2′-azobis(2-methylpropionitrile) (AIBN, 99%) were acquired from Aladdin. Sodium tablets were purchased from Jiaxing Changgao New Material Technology Co., Ltd.

4.2 Synthesis of Ti-MOFs power

MIL-125(Ti) was synthesized using a hydrothermal method. For specific methods, refer to previous work. In detail, 2-aminoterephthalic acid was dissolved in dimethylformamide (DMF) and methanol mixed solution in a specific ratio with stirring for 30 min. Then, tetrabutyl titanate was added to the mixed solution with further stirring for 1 h. After that, the mixed solution was transferred to an autoclave and maintained at 150 °C for 24 hours. The obtained sample was centrifuged multiple times and then vacuum-dried at 60 °C. Finally, MIL-125(Ti) was obtained as a white powder.

4.3 Preparation of the quasi-solid-state polymer electrolytes

Initially, 0.55098 g $NaClO_4$ and 5 mg Ti-MOFs powder were dissolved in the solution mixed with 4.05 g PC, 0.45 g FEC, 0.475 g PEGDA, 25 mg PETEA and 5 mg AIBN (donated as Ti@GPE). The mixture was stirred at room temperature until complete dissolution, resulting in a clear solution. LE was prepared by dissolving 0.55098 g $NaClO_4$ in 5 g PC. GPE was prepared by replacing FEC in Ti@GPE with an equal mass of PC without adding Ti-MOFs. The whole process was carried out in an argon-filled glove box (O_2 < 0.1 ppm, H_2O < 0.1 ppm). These assembled batteries using the above three precursor solution were triggered by an initiator at 70 °C after 3 hours.

4.4 Preparation of the electrode

PBAs active materials was prepared according to our previous study. The cathode electrode was prepared by mixing PBAs active material, Super P and polyvinylidene fluoride (PVDF) in a mass ratio of 7 : 2 : 1 with a certain amount of *N*-methyl-2-pyrrolidone (NMP) for a homogeneous slurry. Then, the slurry was coated onto an aluminum foil with a 200 μm blade and dried at 110 °C for 12 h in vacuum. The cathode was punched into a round pellet with a diameter of 14 mm and the mass loading of PBAs active material was about 1.2 mg cm^{-2}.

4.5 Materials characterization

Fourier transform infrared (FT-IR) spectra were obtained by ta he Nicolet iS10 FTIR spectrometer in the range of 4000 to 400 cm^{-1}. The number of scans was 32 and the resolution for FT-IR measurements was 4 cm^{-1}. All FT-IR spectra were analyzed by Origin software. The phase structures of Ti-MOFs and PBAs cathodes were identified by X-ray diffraction (XRD, Rigaku Ultima diffractometer with Cu Kα radiation, $\lambda = 1.5418$ Å). The N_2 adsorption–desorption isotherms and pore size distribution of Ti-MOFs were measured on a Micromeritics ASAP2460. The tensile property was tested with a universal material testing machine Instron-5592 at a moving speed of 100 mm min^{-1}. Thermogravimetric analysis (TGA) was done with a heating rate of 5 °C min^{-1} in N_2 atmosphere from 30 to 700 °C. The dissolved transition metals on separators were tested by inductively coupled plasma (ICP) spectrometry using an Agilent 5110.

4.6 Electrochemical measurement

Electrochemical impedance spectroscopy (EIS), linear sweeping voltammetry (LSV), and cyclic voltammetry (CV) were performed on an electrochemical workstation (Autolab instrument PGSTAT302N). The AC signal ranging from 0.01 Hz to 100 kHz was used for all the EIS tests. The sodium tablets and Al foil were used as the counter, reference and working electrodes, respectively, for the LSV test with a scanning rate of 1 mV s^{-1}. CV tests were in the voltage range of −0.5–1.5 V with a scanning rate of 0.5 mV s^{-1}. Galvanostatic charge/discharge (GCD) cycling tests were carried out on a LAND CT2100A. DRT analysis was performed using DRT tools.[56] The ionic conductivity (σ) of the electrolytes was also measured by EIS. The polymer electrolytes were sandwiched between polished Al foils in a glove box. The ionic conductivity was calculated according to the following equation:

$$\sigma = \frac{L}{S \times R}$$

where L (cm) represents the thickness of the electrolytes, S (cm^2) is the area of the Al foil, and R (Ω) refers to the bulk resistance of the electrolyte membrane measured by EIS.

Data availability

All relevant data are within the manuscript and its additional files. The data that support the findings of this study are available from the corresponding author upon reasonable request.

Author contributions

Xinyu Wang: conceptualization, visualization, data curation, software, writing-original draft, validation, formal analysis, investigation. Cheng Yang: project administration, writing-review & editing. Ning Jiang: visualization, software. Yichao Wang: formal analysis. Shouyu Sun: formal analysis. Yu Liu: resources, supervision, funding acquisition, writing-review & editing.

Conflicts of interest

The authors declare that they have no known competing financial interests or personal relationships that could have appeared to influence the work reported in this paper.

Acknowledgements

Talents Program, K. C. Wong Pioneer Talent Program, China Three Gorges Corporation (No. WWKY-2021-0027, 202103401), Inner Mongolia Science & Technology Plan (No. 2021ZD0033) and the National Natural Science Foundation of China (Grant No. 52202121). The authors also extend their gratitude to Mr Wang from Shiyanjia Lab (**https://www.shiyanjia.com**) for the XPS analysis.

References

1 Z. Sun, K. Zhu, P. Liu, X. Chen, H. Li and L. Jiao, *Angew. Chem., Int. Ed.*, 2022, **61**, e202211866.
2 Z. Lu, H. Yang, Y. Guo, P. He, S. Wu, Q.-H. Yang and H. Zhou, *Angew. Chem., Int. Ed.*, 2022, **61**, e202206340.
3 P. Liu, H. Yi, X. Chen, K. Zhu, Z. Li, Z. Sun and L. Jiao, *Acc. Mater. Res.*, 2022, **3**, 672–684.
4 Q. Li, D. Yang, H. Chen, X. Lv, Y. Jiang, Y. Feng, X. Rui and Y. Yu, *SusMat*, 2021, **1**, 359–392.
5 Y. Li, F. Wu, Y. Li, M. Liu, X. Feng, Y. Bai and C. Wu, *Chem. Soc. Rev.*, 2022, **51**, 4484–4536.
6 D. Ba, Q. Gui, W. Liu, Z. Wang, Y. Li and J. Liu, *Nano Energy*, 2022, **94**, 106918.

7 G. Gao, D. Tie, H. Ma, H. Yu, S. Shi, B. Wang, S. Xu, L. Wang and Y. Zhao, *J. Mater. Chem. A*, 2018, **6**, 6675–6684.
8 X.-F. Guo, Z. Yang, Y.-F. Zhu, X.-H. Liu, X.-X. He, L. Li, Y. Qiao and S.-L. Chou, *Small Methods*, 2022, **6**, 2200209.
9 H. Wang, Z. Pan, H. Zhang, C. Dong, Y. Ding, Y. Cao and Z. Chen, *Small Methods*, 2021, **5**, 2100372.
10 Y. Zou, G. Liu, Y. Wang, Q. Li, Z. Ma, D. Yin, Y. Liang, Z. Cao, L. Cavallo, H. Kim, L. Wang, H. N. Alshareef, Y.-K. Sun and J. Ming, *Adv. Energy Mater.*, 2023, **13**, 2300443.
11 N. Jiang, C. Yang, Y. Wang, X. Wang, J. Liu and Y. Liu, *Energy Storage Mater.*, 2023, **63**, 102978.
12 N. Jiang, J. Liu, Y. Wang, X. Wang, C. Yang and Y. Liu, *Nano Energy*, 2024, **128**, 109842.
13 Z. Ren, M. Wang, S. Chen, J. Liu, Z. Zhao, H. Li, Z. Chen, D. Wang and X. Liu, *Energy Storage Mater.*, 2023, **60**, 102815.
14 J. Liu, Y. Wang, N. Jiang, B. Wen, C. Yang and Y. Liu, *Angew. Chem., Int. Ed.*, 2024, e202400214.
15 Y. Wang, J. Liu, N. Jiang, J. Yang, C. Yang and Y. Liu, *Small*, 2024, 2403211.
16 J. Song, L. Wang, Y. Lu, J. Liu, B. Guo, P. Xiao, J.-J. Lee, X.-Q. Yang, G. Henkelman and J. B. Goodenough, *J. Am. Chem. Soc.*, 2015, **137**, 2658–2664.
17 C. Chen, T. Li, H. Tian, Y. Zou and J. Sun, *J. Mater. Chem. A*, 2019, **7**, 18451–18457.
18 Y. Wang, N. Jiang, J. Liu, S. Sun, X. Wang, J. Yang, C. Yang and Y. Liu, *Adv. Funct. Mater.*, 2024, 2406809.
19 F. Li, X. Gu, A. Cui, Y. Li, S. Dong, S. Wu, Z. Cheng, Q. Yao, J. Yang and M. Wu, *Adv. Funct. Mater.*, 2024, **34**, 2313146.
20 Q. Song, Z. Li, S. Gan, W. Dong, W. Wang, J. Zhang and Q. Yu, *J. Mater. Chem. A*, 2023, **11**, 1532–1550.
21 J. Liu, C. Yang, B. Wen, B. Li and Y. Liu, *Small*, 2023, **19**, 2370387.
22 X. Liu, H. Gong, C. Han, Y. Cao, Y. Li and J. Sun, *Energy Storage Mater.*, 2023, **57**, 118–124.
23 W. Shu, J. Li, G. Zhang, J. Meng, X. Wang and L. Mai, *Nano-Micro Lett.*, 2024, **16**, 128.
24 L. Chen, W. Sun, K. Xu, Q. Dong, L. Zheng, J. Wang, D. Lu, Y. Shen, J. Zhang, F. Fu, H. Kong, J. Qin and H. Chen, *ACS Energy Lett.*, 2022, **7**, 1672–1678.
25 M. Cui, Y. Zhu, H. Lei, A. Liu, F. Mo, K. Ouyang, S. Chen, X. Lin, Z. Chen, K. Li, Y. Jiao, C. Zhi and Y. Huang, *Angew. Chem., Int. Ed.*, 2024, **63**, e202405428.
26 Q. Liu, Z. Chen, Y. Liu, Y. Hong, W. Wang, J. Wang, B. Zhao, Y. Xu, J. Wang, X. Fan, L. Li and H. B. Wu, *Energy Storage Mater.*, 2021, **37**, 521–529.
27 C. Zhao, Z. Yang, X. Zhou, Z. Hao, J. Chen, Z. Wang, X. Chen, X. Wu, L. Li, L. Li, L. Jiao and S. Chou, *Adv. Funct. Mater.*, 2024, **34**, 2303457.
28 X. Zhou, Q. Zhang, Z. Zhu, Y. Cai, H. Li and F. Li, *Angew. Chem., Int. Ed.*, 2022, **61**, e202205045.
29 S. Wu, Z. Yu, X. Nie, Z. Wang, F. Huang and Q. Wei, *Adv. Energy Mater.*, 2022, **12**, 2202930.
30 X. Xu, K. Lin, D. Zhou, Q. Liu, X. Qin, S. Wang, S. He, F. Kang, B. Li and G. Wang, *Chem*, 2020, **6**, 902–918.
31 Z. Li, X.-Y. Zhou and X. Guo, *Energy Storage Mater.*, 2020, **29**, 149–155.
32 J. Lin, H. Peng, P. Huang, T. Naren, C. Liang, G. Kuang, L. Chen, C. Zhang and W. Wei, *Adv. Funct. Mater.*, 2023, **33**, 2307061.
33 J. Sheng, Q. Zhang, C. Sun, J. Wang, X. Zhong, B. Chen, C. Li, R. Gao, Z. Han and G. Zhou, *Adv. Funct. Mater.*, 2022, **32**, 2203272.
34 Y.-N. Zhou, Z. Xiao, D. Han, L. Yang, J. Zhang, W. Tang, C. Shu, C. Peng and D. Zhou, *Adv. Funct. Mater.*, 2022, **32**, 2111314.
35 Q. Liu, L. Yang, Z. Mei, Q. An, K. Zeng, W. Huang, S. Wang, Y. Sun and H. Guo, *Energy Environ. Sci.*, 2024, **17**, 780–790.
36 T. Duan, H. Cheng, Y. Liu, Q. Sun, W. Nie, X. Lu, P. Dong and M.-K. Song, *Energy Storage Mater.*, 2024, **65**, 103091.
37 F. Tao, X. Wang, S. Jin, L. Tian, Z. Liu, X. Kang and Z. Liu, *Adv. Mater.*, 2023, **35**, 2300687.
38 R. Pietro, C. Luca, S. Luigi, L. Ruirui, E. Stefano, M. Gabriele, G. Sebastiano, M. Luca, I. Plinio, M. Xiaojie and W. Bo, *Appl. Catal., B*, 2024, **345**, 123692.
39 M. Dan-Hardi, C. Serre, T. Frot, L. Rozes, G. Maurin, C. Sanchez and G. Férey, *J. Am. Chem. Soc.*, 2009, **131**, 10857–10859.
40 X. Song, J. He, Y. Wang, J. Wang and S. Zhang, *J. Colloid Interface Sci.*, 2023, **645**, 918–932.
41 M. Yang, F. Feng, J. Guo, R. Wang, J. Yu, J. Ren, Z.-F. Ma, S. Chen and T. Liu, *Energy Storage Mater.*, 2024, **70**, 103492.
42 X. Li, Y. Zheng, Y. Duan, M. Shang, J. Niu and C. Y. Li, *Nano Lett.*, 2020, **20**, 6914–6921.
43 H. Gao, N. S. Grundish, Y. Zhao, A. Zhou and J. B. Goodenough, *Energy Mater. Adv.*, 2021, 1932952.
44 K. Liu, P. Bai, M. Z. Bazant, C.-A. Wang and J. Li, *J. Mater. Chem. A*, 2017, **5**, 4300–4307.
45 S. Zou, Y. Yang, J. Wang, X. Zhou, X. Wan, M. Zhu and J. Liu, *Energy Environ. Sci.*, 2024, **17**, 4426–4460.
46 W. Wang, M. Ding, S. Chen, J. Weng, P. Zhang, W. Yuan, A. Bi and P. Zhou, *Chem. Eng. J.*, 2024, **491**, 151989.
47 M. Zhu, X. Zheng, L. Li, X. Zhu, Z. Huang, G. Wang, Y. Zhang, H. Liu, F. Yu, L. Wen, H.-K. Liu, S.-X. Dou and C. Wu, *Energy Storage Mater.*, 2022, **48**, 466–474.
48 X. Wang, C. Yang, L. Yao, Y. Wang, N. Jiang and Y. Liu, *Adv. Funct. Mater.*, 2024, **34**, 2315007.
49 G. Wang, Y. Wang, L. Yao, J. Yang, X. Chi and Y. Liu, *Energy Storage Mater.*, 2024, **70**, 103530.
50 W. Zhang, Y. Lu, L. Wan, P. Zhou, Y. Xia, S. Yan, X. Chen, H. Zhou, H. Dong and K. Liu, *Nat. Commun.*, 2022, **13**, 2029.
51 Y. Lu, W. Zhang, S. Liu, Q. Cao, S. Yan, H. Liu, W. Hou, P. Zhou, X. Song, Y. Ou, Y. Li and K. Liu, *ACS Nano*, 2023, **17**, 9586–9599.
52 S. Li, H. Zhu, Y. Liu, Z. Han, L. Peng, S. Li, C. Yu, S. Cheng and J. Xie, *Nat. Commun.*, 2022, **13**, 4911.
53 Y. Lu, C.-Z. Zhao, J.-Q. Huang and Q. Zhang, *Joule*, 2022, **6**, 1172–1198.
54 J. P. Schmidt, T. Chrobak, M. Ender, J. Illig, D. Klotz and E. Ivers-Tiffée, *J. Power Sources*, 2011, **196**, 5342–5348.
55 L. U. Subasinghe, G. Satyanarayana Reddy, A. Rudola and P. Balaya, *J. Electrochem. Soc.*, 2020, **167**, 110504.
56 T. H. Wan, M. Saccoccio, C. Chen and F. Ciucci, *Electrochim. Acta*, 2015, **184**, 483–499.